Formation of omega phase induced by laser shock peening in Ti-17 alloy

Si Chen[a], Juan Mu[a,1], Yandong Wang[a,b,**], Minghe Zhang[b], Yang Ren[c], Zhibin An[d]

[a] School of Materials Science and Engineering, Northeastern University, Shenyang 110819, China

[b] School of Materials Science and Engineering, University of Science and Technology Beijing, Beijing 100083, China

[c] X-ray Science Division, Argonne National Laboratory, Argonne, IL 60439, USA

[d] Science and Technology on Plasma Dynamics Laboratory, Air Force Engineering University, Xi'an 710038, China

[**] Correspondence to: Y. Wang, School of Materials Science and Engineering, Northeastern University, Shenyang 110819, China. E-mail addresses: muj@atm.neu.edu.cn (J. Mu), ydwang@mail.neu.edu.cn (Y. Wang).

ABSTRACT

Synchrotron-based high-energy X-ray diffraction and transmission electron microscopy were used to study the in-depth compressive residual strains and microstructure evolution in Ti-17 alloy subjected to two-sided laser shock peening (LSP). A noticeable difference was observed in the lattice strains and extents of peak broadening on the two sides of the sample. The compressive residual strain was smaller and the peak broadening was more pronounced on the bottom surface in comparison to the top surface. This is due to the β→ω phase transformation induced by LSP on the bottom surface. It was determined that the ω phase with fine particle morphology and incommensurate structure is located mainly in the 15 μm-thick layer under the bottom surface. The formation of the LSP-induced ω phase on the bottom surface can be attributed to the adiabatic increase in temperature due to the higher shock peak pressure on the bottom surface, and can result in the relaxation of the accumulated residual compressive strain in the original phases.

Keywords: Laser shock peening; Ti-17; Residual strain; Phase transformation; Strain relaxation; Synchrotron-based high-energy X-ray diffraction

1. Introduction

Titanium alloys have been employed in a wide variety of fields, such as in aerospace, chemical, and biomedical applications, owing to their three main properties: high specific strength, good corrosion resistance, and exceptional biocompatibility [1]. In these applications, titanium alloys are often subjected to fatigue loading. Thus, studies focusing on the improvement of the fatigue property of titanium alloys has become a major area of research. Laser shock peening (LSP), which is a surface treatment technology, has proven to be effective in improving the fatigue property of titanium alloys, such as Ti-6Al-4V [2], Ti–2.5Cu [3], TIMETAL LCB [3] and TC11 [4]. The beneficial effects on the fatigue property are mainly due to the LSP-induced compressive residual stress in the surface layer with large depth, which delays the development of fatigue cracking [5].

In addition to the compressive residual stress, LSP can induce microstructural modifications near the surface [6,7], which can also enhance the fatigue property. For example, the sub-surface dislocation tangle in Ti-6Al-4V induced by LSP can remain stable during isothermal fatigue and thus fatigue lives are extended at elevated temperature [8]. Therefore, in recent years, the LSP-induced microstructural modification of titanium alloys has attracted significant attention. Dislocation structures [8], deformation twins [9], and grain refinement (including subgrain refinement [10], nanograin refinement [4]) can be found in titanium alloys following the LSP treatment. For example, Yang et al. [11] investigated the microstructure characteristics of Ti-17 alloy subjected to LSP, and found gradient microstructures with nanocrystalline grains on the surface, dislocations and subgrains close to the surface, and dislocations and deformation twins near the substrate.

However, phase transformation induced by LSP in titanium alloys has rarely been observed. A small amount of inverse-transformation martensite ($\alpha \rightarrow \alpha'$) was found and may be induced by local shear under the ultra-strong mechanical effect of the laser shock wave for CP titanium [9]. Contrary to this, the phase transformation behaviors in titanium alloys are very common under similar conditions as those of shock loading. Martensitic ($\beta \rightarrow \alpha''$) [12,13] and omega ($\alpha \rightarrow \omega$) [14,15] phase transformations induced by shock loading can be observed when the amplitude of the shock wave is sufficiently high. However, the β (body-centered cubic structure) $\rightarrow$ ω (hexagonal structure) phase transformation induced by shock loading has not been observed in titanium alloys, but it was observed in other alloys with body-centered cubic structure, such as Ta [16] and Zr [17]. At the same time, the occurrence of phase transformation can induce stress relaxation in the original phase [18]. Thus, when titanium alloys are subjected to LSP, it comes up with some unanswered questions: Whether phase transformation occurs or not? What kind of phase transformation can occur? What is the influence of phase transformation on the residual stress?

In the present study, an in situ synchrotron-based high-energy X-ray diffraction (HE-XRD) method was used to investigate the in-depth compressive residual strains and microstructure evolution after the two sided LSP treatment of Ti-17 alloy. The ω phase induced by LSP in the titanium alloy was observed for the first time and further characterized by transmission electron microscopy (TEM). The formation mechanism of the LSP-induced ω phase and the interaction between the residual strain and phase transformation are systematically discussed.

2. Materials and methods

The material investigated in the present study is a Ti-17 alloy, which is a "beta-rich" α + β titanium alloy with nominal chemical composition Ti-5Al-2Sn-2Zr-4Mo-4Cr in wt%. The actual chemical composition with an obvious fluctuation of the investigated alloy is listed in Table 1. The specimen used in the studies was obtained in a sheet form with a thickness of 5 mm. Two-sided LSP treatment was performed simultaneously on both sides of the sample under the similar condition with only one difference. The processing parameters generated by a Qswitched neodymium-doped yttrium aluminum garnet (Nd:YAG) laser were the same as follows: wavelength of 1064 nm, frequency of 2 Hz, laser pulse energy of 3 J, pulse duration of 20 ns, spot diameter of 2.2 mm, spot overlap of 50%, and surface coverage of 60%. Transparent confining layer and thermo-protective coating layer were flowing water and black tape (0.7 mm thick), respectively. The only difference was the thickness of the water-confining layer (1 mm for the top side and 2 mm for the bottom side). It is convenient to adjust the thickness of the water-confining layer. Thus, it was set as the only variable for comparison of the outcomes from two sides. The microstructures of the specimen before and after the LSP treatment were characterized by scanning electron microscopy (SEM) and TEM. The SEM samples were prepared by mechanically grinding and polishing, and followed by etching with Kroll's reagent ($2HF:4HNO_3:94H_2O$). The TEM samples were prepared by mechanically grinding and ion milling the side far from surface, to obtain thin plates with a thickness of ~30 μm and to prevent the destruction of the required surface.

The specimen used for the HE-XRD studies was cut into a sample of size, $25 \times 5 \times 1$ mm^3 from the LSP-treated sample. The HE-XRD measurements were performed on the 11-1D-C beamline of the Advanced Photon Source at the Argonne National Laboratory. A schematic of the geometry for the HE-XRD measurements is shown in Fig. 1. The sample was irradiated with high-energy X-rays with an energy of 105.6 KeV (wavelength 0.117418 Å) and a beam size of 0.2×0.2 mm^2, and two-dimensional (2D) diffraction patterns were recorded using a 2D detector (Perkin Elmer amorphous silicon). The incident beam was scanned along the dashed line as indicated in Fig. 1, from the peened surface (gray area) on one side to the peened surface area on the other side, with a step size of 50 μm. The Fit2D software was used to process the 2D diffraction patterns. One-dimensional (1D) diffraction profiles of the longitudinal direction (LD, parallel to the peened surface, azimuth angle $\varphi = 90°$) and the transverse direction (TD, perpendicular to the peened surface, $\varphi = 0°$) were obtained by integrating along the specified azimuth angle over a range of ±

5° in the 2D diffraction patterns. The lattice strain of different crystallographic planes, ε_{hkl}, was calculated from the relative change in the measured inter-planar spacing, d_{hkl}, given by $\varepsilon_{hkl} = (d_{hkl} - d_0)/d_0$. The reference lattice spacing, d_0, was obtained from the strain-free sample, which was a small pillar of the original Ti-17 material acquired prior to the LSP treatment.

3. Results

3.1. Microstructure of the original material

The 1D HE-XRD profile integrated over the entire 360° azimuthal range for the original Ti-17 material acquired prior to the LSP treatment is shown in Fig. 2(a). The diffraction pattern indicates that the original material is composed of two phases: the β phase with a body-centered cubic structure and the α phase with a hexagonal close-packed structure. Using these diffraction peaks, the lattice parameters of the two phases were calculated as a = 3.2303 Å for the β phase and a = 2.9309 Å and c = 4.6852 Å for the α phase, respectively. Fig. 2(b) shows a SEM micrograph of the original microstructure of the Ti-17 alloy. It shows a bimodal microstructure with equiaxed primary α grains (characterized as αp in the picture, dark gray) and lamellar secondary α (characterized as αs, dark gray) distributed in a metastable β matrix (light gray). However, contrary to the expectations, the microstructure is not uniform. The range of the grain size of α_p phase is 0.5–5.0 μm and the αs phase is embedded inhomogeneously in the β matrix.

3.2. In situ HE-XRD characterization of the LSP-treated sample

During the LSP treatment, when the laser shock waves propagate into the material, plastic deformation occurs and results in residual compressive strain. The measured in-depth residual lattice strains along the LD after the LSP treatment are shown with error bars in Fig. 3(a). Error bars indicate the standard deviation and most of the error values are quite small except in the $\{110\}_\beta$, orientation, as the peak of $\{110\}_\beta$ was fitted together with two neighboring peaks. The results show large gradient lattice strains on both sides of the sample. With an increase in the distance, compressive near-surface lattice strains on one side decrease gradually, then become to balancing tensile strains, and subsequently change to compressive near-surface strains on the opposite side. The compressive residual strain induced by LSP can be as high as 6400 με and the affected depth is ~400–850 μm. The residual strains of both phases show a strong orientation dependence, which indicates the presence of grain-orientation-dependent residual stress or inter-granular stress in the LSP-treated sample [19]. The orientation $\{200\}_\beta$ accumulates the largest compressive residual strain at the surface and the largest change of lattice strain across the sample thickness, indicating that it is the most compliant orientation in both phases, which is consistent with a previous report [20]. All α orientations accumulate significantly smaller residual lattice

strains than the $\{200\}_\beta$ orientation, and the smallest value of compressive residual strain at the surface results from the stiffest $\{0002\}_\alpha$ orientation.

There is a noticeable difference in the lattice strains on the two sides. The magnitude of the compressive residual strains on the bottom side is smaller than that on the top side. Contrary to this, the affected depth of compressive strains on the bottom side is larger than that on the top side. Additional uncharacteristic phenomena occur at the bottom surface and these can be clearly seen at the inset in Fig. 3(a). As the distance to the bottom surface increases, the compressive residual strains slowly decrease in the 50 μm region below the surface. With the further increase of the distance, the compressive residual strains drop sharply until they reach the maximal affected depth. In addition, the maximum values of the compressive residual strains of the $\{0002\}_\alpha$ and $\{10\bar{1}1\}_\alpha$ orientations were obtained in the sub-surface (50 μm from the bottom surface). As both sides of the sample were LSP-treated under the similar condition with only one difference, the in-depth compressive residual strain distribution near both surfaces due to the LSP is expected to be similar. These uncharacteristic residual strains indicate an unexpected phenomenon at the bottom surface.

Fig. 3(b) shows the lattice strain profiles along the TD as a function of the distance from the peened surface. They follow an opposite trend to the lattice strains along the LD. The tensile strains on the surface are gradually decreased with an increase in the distance. Some orientation drop so fast in the strain that they are changed to compressive strains. The $\{200\}_\beta$ orientation still accumulates the largest change of the strain. The strains stay constant in the middle of the sample, and revert to the tensile strains at the opposite surface. This opposite trend is consistent with the Poisson's effect.

To obtain additional insights into the behavior of the residual strain after the LSP treatment, the in-depth diffraction peak broadening was studied. The full width at half maximum (FWHM) of the diffraction peaks as a function of depth is shown in Fig. 3(c). The FWHM value also reveals a considerable grain-orientation-dependent anisotropy. The orientation, $\{0002\}_\alpha$, features the minimum FWHM value, while the two orientations of the β phase, $\{200\}_\beta$ and $\{211\}_\beta$, feature a rather high FWHM value. Furthermore, the peak broadening near the bottom surface is noticeable. When the distance towards the bottom surface increases, the FWHM value of most of the lattice planes increases gradually in the 200 μm region below the bottom surface and then begins to decrease until it becomes flat. There are several known factors affecting the peak broadening. The possible reason for the peak broadening on both sides is the microstrain and crystal size refinement induced by the similar extent of plastic deformation after LSP treatment; therefore, the in-depth FWHM distributions near both surfaces are expected to resemble each other. However, the uncharacteristic increase in the FWHM value near the bottom surface is not related to the plastic deformation. A possible reason for the peak broadening near the bottom surface can be a newly formed phase with a small crystallite size. This can also explain the uncharacteristic residual strains near the bottom surface.

3.3. Microstructure characterization of the newly formed phase

As mentioned before, LSP can induce microstructural modification near the surface. Fig. 4 is the cross-sectional SEM micrographs of the LSP-treated sample near two surfaces. There is no obvious grain refinement of two original phases in the near-surface layer. The color of the near-surface layer is darker than the substrate due to lots of structural defects (such as dislocations and sub-boundaries) induced by LSP [21]. This layer is also called severe plastic deformation (SPD) layer. It can be clearly seen that the SPD layer on the bottom side is thicker than that on the top side, in relation to the larger affected depth of compressive strains on the bottom side, which will be discussed later. The thicknesses of severe plastic deformation layers are ~60 μm for the top side and ~80 μm for the bottom side, respectively. In addition, no new phase was found in the SEM micrographs.

However, a newly formed phase was identified on the bottom side by 2D HE-XRD patterns, which was a bright spot located near the $\{110\}_\beta$ diffraction ring, as shown in Fig. 5(a). There is also an additional diffraction peak near the $\{200\}_\beta$ peak but with rather low intensity, which can be seen in the inset of Fig. 5(a). The newly formed phase may be a martensite or an omega phase due to their specific position (near the diffraction rings of the β phase). The first additional peak near $\{110\}_\beta$ can be characterized as $(101)_\omega$ or $(002)_{\alpha''}$. But the second additional peak near $\{200\}_\beta$ is more possible from the omega phase, i.e., $(201)_\omega$, rather than from the martensite phase. Furthermore, TEM analysis was performed to identify the newly formed phase.

Fig. 5(b) shows a selected-area electron diffraction pattern of the LSP-treated bottom surface along the $\langle 110\rangle_\beta$ zone axis, from which βphase-associated spots as well as clear extra spots related to the newly formed phase (indicated by arrows) can be observed. As shown in the inset of Fig. 5(b), the dark-field electron micrograph derived from one extra spot confirms that the newly formed phase is uniformly distributed in the β matrix with fine, nanometer-sized particle morphology. Such small grain size of the ω phase is beyond the spatial resolution of SEM. The extra spots and the fine morphology indicate that the newly formed phase is the ω phase.

However, the orientation of the ω phase is shifted from the well-established $(0001)_\omega \parallel (111)_\beta$; $[11\bar{2}0]_\omega \parallel [1\bar{1}0]_\beta$ orientation relationship. The reflections of two ω variants (indicated by a circle) are located on the faint circular diffuse streaks, but not in the commensurate positions of 1/3 and 2/3 $(1\bar{1}2)_\beta$. Instead, the positions of these reflections are shifted towards each other. The reflections of the other two ω variants are expected to be obscured by the β matrix reflections. However, distinct ω reflections can be seen outside the $(1\bar{1}2)_\beta$ and $(002)_\beta$ reflections as shown. This incommensurate structure of the ω phase has been observed in other titanium alloys [22–24], and its origin is discussed later.

3.4. Detailed HE-XRD investigation of the ω phase

For the better understanding of the ω phase on the bottom surface induced by LSP, it was investigated in detail. Thus, the volume fraction and lattice strain of the ω phase were analyzed. Fig. 6(a) shows the 1D HE-XRD profiles integrated along the specific azimuth angle as shown in Fig. 5(a). The range of the specific azimuth angle fully covers the bright spot of the ω phase. As the intensities of diffraction spots of the ω phase are quite low, apart from the bright spot, it is enough to use the bright spot to obtain detailed information on the ω phase. It can be seen that the intensities of the α and β phases increase gradually with the increase in the distance from the bottom surface, while the variation in the intensity of the $\{10\bar{1}1\}_{\omega}$ peak is rather complex. The change in the intensities of the α and β phases is related to the volume of the phase diffracted in the sample area covered by the beam. For the better understanding of the change in the sample area covered by the beam, a schematic route of beam movement is shown in the Fig. 6(b). The beam (200 μm × 200 μm) moved across the bottom surface from the air to the material with a step size of 50 μm. As the α phase is not involved in the β→ω phase transformation, its volume fraction in unit area can be considered constant; thus, its intensity is expected to depend linearly on the beam-covered area. Therefore, the beam-covered area is calculated to verify the location of the beam center with respect to the bottom surface. The integrated intensities for the $\{0002\}_{\alpha}$, $\{1011\}_{\omega}$, $\{110\}_{\beta}$, and $\{10\bar{1}1\}_{\alpha}$ peaks along with the calculated intensities of the α phase are indicated in Fig. 6(c), where the calculated location of each beam center is shown on the horizontal axis. The corresponding calculated fit of the intensities is in good agreement with the experiment data of the α phase.

The integrated intensity of the $\{10\bar{1}1\}$ plane of the ω phase increases noticeably when the distance from the beam center to the sample surface increases to the level of −85 μm, then gradually increases until it becomes flat at −35 μm, 15 μm, and 65 μm, and finally decreases significantly at 115 μm. It should be noted that a sum of the intensities at −85 μm and 115 μm is approximately equal to the intensity at 15 μm, which indicates that the volume fraction of the ω phase at 15 μm is the sum of those at −85 μm and 115 μm. In addition, the maximum intensity is approximately four times the intensity at 115 μm. These results explain the in-depth distribution of the ω phase below the bottom surface, as shown in Fig. 6(b). The maximum intensity of the ω phase at a distance of 15 μm from the beam center to the sample surface, where there is a layer with a thickness of 65 μm below the bottom surface, is donated by the total volume fraction of the ω phase, while 80% of the ω phase is distributed homogeneously in the 15 μm-thick layer below the bottom surface. Such a narrow distribution region indicates that the effect on ω phase formation is restricted very close to the bottom surface.

The changes in compressive lattice strains of $\{0002\}_{\alpha}$, $\{110\}_{\beta}$, and $\{10\bar{1}1\}_{\alpha}$ planes near the two surfaces in the LD are compared in Fig. 6(d). In comparison to the compressive residual strains on the top side, it can be seen that the magnitude of the compressive residual strains on the bottom

side is smaller and the affected depth of those is larger. In addition, the changes in the compressive strain in the 200 μm thick layer below the surface on two sides are quite different. With the increase in the depth, compressive strain on the top side decreases gradually. Contrary to this, compressive strain on the bottom side either stays constant or increases a little and then decreases, which results in the maximum value of the compressive strain on the sub-surface rather than the surface. This can be attributed to the strain accommodation of hard ω particles on the bottom surface. Fig. 6(d) also shows the evolution of the tensile lattice strain of the $\{10\bar{1}1\}_{\omega}$ plane on the bottom side. When calculating the lattice strain of the $\{10\bar{1}1\}_{\omega}$ plane, the reference d_0 can be calculated from the theoretical lattice parameters of the ω phase. From well-established geometric assumptions, $a_{\omega} = \sqrt{2}a_{\beta}$ and $c_{\omega} = \frac{\sqrt{3}}{2}a_{\beta}$ [25], the theoretical lattice parameters for the ω phase can be calculated as a = 4.5684 Å and c = 2.7975 Å from the original lattice parameters for the β phase. The tensile lattice strain gradually decreases as the distance from the bottom surface increases, which indicates a retarded restraint from the surrounding phase corresponding to the decrease of the compressive residual strain of the original phases.

4. Discussion

It is well-known that the athermal ω phase with dispersed particle morphology can be easily obtained by quenching in Ti-17 alloy. However, the material used in this study has a steady bi-modal microstructure without any athermal ω phase before the LSP treatment. Thus, the ω phase occurring near the bottom surface is solely related to the LSP treatment.

As the laser shockwaves propagate from the peened surface to the interior of the target material, plastic deformation occurs at a depth where the peak stress no longer exceeds the Hugoniot elastic limit (P_h) of the target material, which induces compressive residual stresses throughout the affected depth. The value of P_h used in this study was 2.8 GPa [26]. According to Fabbro et al. [27], the plastically affected depth L_p can be estimated by

$$L_P = \frac{C_e C_P \tau}{C_e - C_P} \frac{P \pm P_h}{2P_h}, \quad (1)$$

where C_e and C_p are the velocity of elastic and plastic waves, respectively, P is the peak pressure, and τ is pulse duration. The L_p depends linearly on both P and τ. The τ value of both sides remains constant as 20 ns. However, the affected depth of compressive strains on the bottom side are larger than on the top side, which indicates that P value is slightly higher on the bottom surface than on the top surface.

According to the prediction model by Fabbro et al. [28] with a confining medium, the pulsed laser-induced shock peak pressure can be determined by

$$P(\mathrm{GPa}) = 0.01\sqrt{\frac{\alpha}{2\alpha+3}}\sqrt{Z(\mathrm{g/cm^2s})}\sqrt{I_0(\mathrm{GW/cm^2})}, \quad (2)$$

where α is a corrective factor corresponding to the fraction of the internal energy resulting in the increase in the pressure, $Z(2/Z = 1/Z_1 + 1/Z_2)$ is the reduced shock impedance of the confining layer (water) and the target material (Ti-17), and I_0 is the laser power intensity. The acoustic impedances of the water-confining layer and the Ti-17 material are 0.165×10^6 g/cm^2 s and 2.75×10^6 g/cm^2 s, respectively [29]. The laser power intensity can be calculated as $I_0 = \frac{4E}{\tau \pi d^2} = \frac{4 \times 3\ \mathrm{J}}{20\ \mathrm{ns} \times \pi \times (2.2\ \mathrm{mm})^2} \approx 3.946$ GW/cm^2. Factor α varies over the range of 0.2–0.5, and depends on the confining layer and other process conditions [30]. Only the thickness of the water-confining layer is different on both sides and is critical for the peak pressure. When the confining layer is too thin (several micrometers), the confining effect of the peak pressure is not sufficient. When the confining layer is very thick (tens of meters), water absorbs a significant amount of laser energy, resulting in a decrease in the laser intensity at the target surface; thus, the peak pressure decreases. Morales et al. [31] simulated plasma dynamics subjected to LSP conditions (λ = 1064 nm, F = 84 J/cm^2, and FWHM = 9 ns) with different confining layers. It was found that the peak pressure rapidly increased with the increase in the thickness of the water layer until it reached a critical value of ~25 μm. Once the critical value of this thickness was surpassed, the peak pressure increased slowly. Kadhim et al. [32] investigated the effects of water layer thickness on the microhardness when subjected to LSP with a laser wavelength of 1064 nm and pulse duration of 10 ns. The microhardness increased due to the increase in the plasma pressure when the surface and 2 mm on the bottom surface result in different α factors. For the top surface, when α is set to 0.2, the calculated peak pressure is 2.69 GPa. For the bottom surface, when α is set to 0.25, the calculated peak pressure is 2.96 GPa.

In addition, the coating layer is also crucial to the peak pressure when its acoustic impedance is lower than that of the target material. Peyer et al. [33] and Fabbro et al. [34] reported that when an Al coating layer was applied on 316L stainless steels in the water-confined regime, the peak pressure increased by 30–50% in comparison with steels without any coating layer. The increase in the peak pressure is due to the difference in the impedances between the coating and the target materials. They also found that the peak pressure was independent of the type of the coating material. In this study, we used the black tape with low acoustic impedance as the coating material and assumed a pressure increase of 35%. Thus, the peak pressure of the top and bottom surfaces could be increased to 3.63 GPa and 4.0 GPa, respectively.

The differences in the affected depth of the compressive strains and the thickness of the SPD layer on two sides are both related to the peak pressure. As mentioned before, the peak pressure depends linearly on both affected depth and pulse duration. More peak pressure can induce larger affected depth. As the pressure value of the bottom surface is slightly higher than that of the top surface, it is reasonable that a larger affected depth was formed on the bottom side. Nie et al. [21] investigated on the SPD layer with different LSP parameters and found that the more the peak pressure generated, the thicker the SPD layer formed, when the peak value is between the Hugoniot

elastic limit and the threshold for the plasma breakdown. As the peak pressure of two surfaces exceed not too much than the Hugoniot elastic limit, it should be below the threshold for the plasma breakdown. Thus, a slightly higher pressure can induce a thicker SPD layer on the bottom side.

The plastic deformation induced by high peak pressure can be a significant factor in the ω formation mechanism during the LSP treatment. The ω phase, induced by deformation, has various morphologies: (i) plate-shaped ω phase in the β matrix, (ii) plate-like ω phase via mechanical twinning, and (iii) fine ω particles in the β matrix. In the current work, the ω phase was determined to be nano-sized fine particles. These three cases are discussed in the following.

The plate-shaped ω phase in the β matrix has been observed in metastable β titanium alloys [35,36] after severe plastic deformation; it is assumed that its formation is based on shear deformation. It was also found in β-stabilized alloys shocked under such a high pressure. Hsiung et al. [16] reported that a plate-shaped ω phase was formed in Ta-based alloys shocked at 45 GPa. Dey et al. [17] investigated a plate-shaped ω phase in ZreNb alloy shocked at 14.5 GPa. In this study, the laserinduced shock pressure of 4.03 GPa was possibly not sufficiently high to induce plate-shaped ω in Ti-17 alloy.

Plate-like ω phase via mechanical twinning has been reported by several researchers. Hanada et al. [37,38] reported that a plate-like single variant of ω phase could be preferentially induced in a {332} ⟨113⟩ twin. Sukedai et al. [39] and Lai et al. [40] identified a plate-like ω phase along the {112}⟨111⟩ twin boundary. However, no deformation twins were found near the bottom surface in the current study, which is in agreement with literature [11]. It was suggested that the strain rate was too high and time was too short to allow the formation of deformation twins during the LSP.

Fine ω particles in the β matrix after deformation have been found in as-quenched TieV and TieCr alloys [41,42]. The as-quenched samples provided an athermal ω phase with fine particle morphology prior to deformation and the size and the number of ω particles increased after the deformation. Zhao et al. [41] reported that even when the athermal ω phase formation was suppressed by increasing the stability of the β phase, cold rolling could still induce a considerable amount of fine ω particles. Liu et al. [42] suggested that the ω phases were induced by cold rolling via the “growth of ω-particles”. These studies suggest that the prior athermal treatment is crucial in the nucleation of the ω phase and the subsequent deformation determines the growth of the ω phase. In this study, there was no athermal ω phase prior to the LSP treatment and the coating layer protected the material surface from direct thermal effects. Thus, it is unclear if LSP can provide similar athermal conditions to nucleate fine ω particles.

Ahmed et al. [43] suggested that the formation of ω particles could be favorable at high strain rates during the compression tests, owing to an increase in the temperature value to the range of

athermal ω formation due to adiabatic heating. The LSP can also cause a noticeable adiabatic temperature increase with a rather high strain rate. The adiabatic temperature increase due to the conversion of plastic deformation to heat can be calculated as

$$\Delta T = \frac{\beta}{\rho C_V} \int_0^{\varepsilon_f} \sigma d\epsilon, \quad (3)$$

where β is the Taylor–Quinney coefficient with a typical value of 0.9 for most metals, ρ is the density and C_V is the specific heat capacity of the target material (ρ = 4.65 g/cm^3 and C_V = 525 J/(Kg K) for Ti-17 alloy), σ is the flow stress, and ε_f is the true strain. Under the LSP condition, the increase in the temperature can be approximated as $\Delta T = \frac{\beta}{\rho C_V} \times P \times \varepsilon = \frac{\beta}{\rho C_V} \times P \times \dot{\varepsilon} t$ [11]. The strain rate $\dot{\varepsilon}$ in LSP typically reaches 10^7/s and the duration t in the water-confined mode is 2–3 times longer than the laser-pulse duration [44]. Therefore, the values of the adiabatic temperature increase on the top and bottom surfaces were calculated as 803 and 885 K, respectively. The temperature of the two surfaces during LSP can reach 828 and 910 °C, respectively. The β transus temperature of the Ti-17 alloy is ~890 °C; thus, the temperature of the bottom surface can reach the temperature of the β phase field, while that of the top surface cannot.

Thus, the formation mechanism of the LSP-induced ω phase can be described as follows. The bottom surface is laser shocked under high pressure, which generates a large plastic deformation resulting in an adiabatic temperature rise to the β phase field, and then the surface is cooled down from the β field due to the cooling effect of the waterconfining medium. The duration of the adiabatic increase in the temperature and the subsequent cooling is in the order of ns. Banerjee et al. [45] suggested that the shock loading experiment was equivalent to the athermal treatment, because the duration of the shock loading was typically in the order of μs, and the diffusive motion of atoms was negligible. As observed in the case of shock loading, the LSP treatment provides conditions similar to the athermal treatment to nucleate fine ω particles. Furthermore, the large plastic deformation induced by the LSP treatment provides ideal conditions for the growth of fine ω particles. Thus, the β → ω phase transformation occurs on the bottom surface after LSP treatment.

The narrow distribution region of the ω phase near the bottom surface can also be described by this mechanism. It is known that the pressure pulse generated by LSP attenuates rapidly when it travels through the material. This results in a rapid decrease in the magnitude of the adiabatic heating as the distance from surface is increasing. Moreover, the temperature of the bottom surface is only slightly higher than that of the β transus. Thus, the temperature sharply drops below that of the β transus within a short distance near the bottom surface, which results in the narrow distribution region of the ω phase.

In addition, it is necessary to draw attention to the incommensurate structure of ω phase, which has been observed in previous reports [22–24] with extensive diffuse scattering streaks and deviated positions of intensity maxima. The extent of the deviation represents the stability of the

ω phase with respect to the β phase and depends on the solute (βstabilizer) content and the extent of undercooling below the ω transformation temperature T_{ω} [25]. As the LSP treatment was applied at room temperature, it means the extent of undercooling is not the crucial factor in this case. In addition, the diffusive motion of atoms, i.e., diffusion controlled solute partitioning, was negligible because of the short duration of the LSP treatment as mentioned before. Thus, the LSP treatment has little effect on the incommensurate structure of the ω phase. However, it has been already reported about the presence of commensurate structure of ω phase in Ti-17 alloy following quenching [46], which means the nominal chemical composition of Ti-17 alloy is enough for commensurate ω phase. This indicates that the observed incommensurate structure of the ω phase in this study can be attributed to the inhomogeneous microstructure of the original material with higher solute content of β-stabilizer on the bottom surface, which is supported by the wide range of actual fluctuated chemical composition of investigated sample. More detailed investigation on the incommensurate structure of the ω phase is needed.

For a certain extent, the compressive strain and the ω phase affect each other simultaneously. On the one hand, the formation of both the compressive strain and the ω phase results from the shock peak pressure. On the other hand, the ω phase can facilitate the release of the accumulated compressive strain, which probably have little negative effects on the enhanced fatigue life improved by the LSP treatment, due to its small volume fraction. Nevertheless, the homogeneously distributed ω phase can result in fine-grained strengthening. The effect of the ω phase on the LSP strengthening needs to be further investigated in detail.

5. Conclusions

The in-depth distribution of the residual strains and the microstructure evolution in the Ti-17 alloy following the two-sided LSP treatment were investigated by HE-XRD and TEM methods. Large residual strain gradients were observed in the near-surface region on both sides. However, there is a distinct difference in the lattice strains and in the extents of peak broadening observed on the top and bottom surfaces. Smaller compressive strain and larger peak broadening occur on the bottom surface compared to those on the top surface, which are induced by the formation of the ω phase. Fine ω particles with incommensurate structure are mainly distributed in the 15 μm-thick layer under the bottom surface. The formation of the ω phase is attributed to the adiabatic increase in the temperature due to the higher shock peak pressure on the bottom surface. The formation of the ω phase can result in the relaxation of the residual compressive strain.

Declaration of competing interest

We declare that we have no financial and personal relationships with other people or organizations that could inappropriately influence (bias) our work.

Acknowledgements

This work was supported by the National Natural Science Foundation of China (Nos. 51771049, 51790484 and 51674082). This research used resources of the Advanced Photon Source, a U.S. Department of Energy (DOE) Office of Science User Facility operated for the DOE Office of Science by Argonne National Laboratory under Contract No. DE-AC02-06CH11357.

Data availability

The raw/processed data required to reproduce these findings cannot be shared at this time as the data also forms part of an ongoing study.

References

[1] C. Leyens, M. Peters, Titanium and Titanium Alloys: Fundamentals and Applications, Wiley, Weinheim, 2003.

[2] J.J. Ruschau, R. John, S.R. Thompson, T. Nicholas, Fatigue crack nucleation and growth rate behavior of laser shock peened titanium, Int. J. Fatigue 21 (1999) S199–S209.

[3] E. Maawad, Y. Sano, L. Wagner, H.G. Brokmeier, C. Genzel, Investigation of laser shock peening effects on residual stress state and fatigue performance of titanium alloys, Mater. Sci. Eng. A 536 (2012) 82–91.

[4] X. Nie, W. He, S. Zang, X. Wang, J. Zhao, Effect study and application to improve high cycle fatigue resistance of TC11 titanium alloy by laser shock peening with multiple impacts, Surf. Coat. Technol. 253 (2014) 68–75.

[5] C.S. Montross, T. Wei, L. Ye, G. Clark, Y.-W. Mai, Laser shock processing and its effects on microstructure and properties of metal alloys: a review, Int. J. Fatigue 24 (10) (2002) 1021–1036.

[6] S. Prabhakaran, S. Kalainathan, Compound technology of manufacturing and multiple laser peening on microstructure and fatigue life of dual-phase spring steel, Mater. Sci. Eng. A 674 (2016) 634–645.

[7] S. Prabhakaran, A. Kulkarni, G. Vasanth, S. Kalainathan, P. Shukla, V.K. Vasudevan, Laser shock peening without coating induced residual stress distribution, wettability characteristics

and enhanced pitting corrosion resistance of austenitic stainless steel, Appl. Surf. Sci. 428 (2018) 17–30.

[8] I. Altenberger, R.K. Nalla, Y. Sano, L. Wagner, R.O. Ritchie, On the effect of deeprolling and laser-peening on the stress-controlled low- and high-cycle fatigue behavior of Ti-6Al-4V at elevated temperatures up to 550 degrees C, Int. J. Fatigue 44 (2012) 292–302.

[9] J.Z. Lu, L.J. Wu, G.F. Sun, K.Y. Luo, Y.K. Zhang, J. Cai, C.Y. Cui, X.M. Luo, Microstructural response and grain refinement mechanism of commercially pure titanium subjected to multiple laser shock peening impacts, Acta Mater. 127 (2017) 252–266.

[10] X. Shen, P. Shukla, P. Swanson, Z. An, S. Prabhakaran, D. Waugh, X. Nie, C. Mee, S. Nakhodchi, J. Lawrence, Altering the wetting properties of orthopaedic titanium alloy (Ti–6Al–7Nb) using laser shock peening, J. Alloys Compd. 801 (2019) 327–342.

[11] Y. Yang, H. Zhang, H. Qiao, Microstructure characteristics and formation mechanism of TC17 titanium alloy induced by laser shock processing, J. Alloys Compd. 722 (2017) 509–516.

[12] M.K. Koul, J.F. Breedis, Strengthening of titanium alloys by shock deformation, in: R.I. Jaffee, N.E. Promisel (Eds.), The Science, Technology and Application of Titanium, Pergamon Press, Oxford, 1970, pp. 817–828.

[13] Y. Ren, F. Wang, S. Wang, C. Tan, X. Yu, J. Jiang, H. Cai, Mechanical response and effects of β-to-α″ phase transformation on the strengthening of Ti–10V–2Fe–3Al during one-dimensional shock loading, Mater. Sci. Eng. A 562 (2013) 137–143.

[14] Y.I. Mescheryakov, A.K. Divakov, Affect of shock-induced phase transformations on dynamic strength of titanium alloys, Int. J. Impact Eng. 26 (1−10) (2001) 497–508.

[15] D.R. Jones, B.M. Morrow, C.P. Trujillo, G.T. Gray, E.K. Cerreta, The α–ω phase transition in shock-loaded titanium, J. Appl. Phys. 122 (4) (2017) 045902.

[16] L.M. Hsiung, D.H. Lassila, Shock-induced deformation twinning and omega transformation in tantalum and tantalum–tungsten alloys, Acta Mater. 48 (20) (2000) 4851–4865.

[17] G.K. Dey, R. Tewari, S. Banerjee, G. Jyoti, S.C. Gupta, K.D. Joshi, S.K. Sikka, Formation of a shock deformation induced ω phase in Zr 20 Nb alloy, Acta Mater. 52 (18) (2004) 5243–5254.

[18] S. Cai, J. Schaffer, Y. Ren, Deformation of a Ti-Nb alloy containing α″-martensite and omega phases, Appl. Phys. Lett. 106 (2015) 131907.

[19] Y.D. Wang, R. Lin Peng, X.L. Wang, R.L. McGreevy, Grain-orientation-dependent residual stress and the effect of annealing in cold-rolled stainless steel, Acta Mater. 50 (7) (2002) 1717–1734.

[20] A.M. Stapleton, S.L. Raghunathan, I. Bantounas, H.J. Stone, T.C. Lindley, D. Dye, Evolution of lattice strain in Ti–6Al–4V during tensile loading at room temperature, Acta Mater. 56 (20) (2008) 6186–6196.

[21] X. Nie, W. He, Q. Li, N. Long, Y. Chai, Experiment investigation on microstructure and mechanical properties of TC17 titanium alloy treated by laser shock peening with different laser fluence, J. Laser Appl. 25 (4) (2013) 042001.

[22] D. De Fontaine, N.E. Paton, J.C. Williams, The omega phase transformation in titanium alloys as an example of displacement controlled reactions, Acta Metall. 19 (11) (1971) 1153–1162.

[23] W. Sinkler, D.E. Luzzi, An electron diffraction investigation of the diffuse ω structure in quenched Ti-3d transition metal alloys, Acta Metall. Mater. 42 (4) (1994) 1249–1260.

[24] N.G. Jones, R.J. Dashwood, M. Jackson, D. Dye, β Phase decomposition in Ti–5Al–5Mo–5V–3Cr, Acta Mater. 57 (13) (2009) 3830–3839.

[25] S.K. Sikka, Y.K. Vohra, R. Chidambaram, Omega phase in materials, Prog. Mater. Sci. 27 (3) (1982) 245–310.

[26] C. Cellard, D. Retraint, M. François, E. Rouhaud, D. Le Saunier, Laser shock peening of Ti-17 titanium alloy: influence of process parameters, Mater. Sci. Eng. A 532 (2012) 362–372.

[27] P. Peyre, R. Fabbro, Laser shock processing: a review of the physics and applications, Opt. Quant. Electron. 27 (12) (1995) 1213–1229.

[28] R. Fabbro, J. Fournier, P. Ballard, D. Devaux, J. Virmont, Physical study of laserproduced plasma in confined geometry, J. Appl. Phys. 68 (2) (1990) 775–784.

[29] K. Ding, FEM simulation of two sided laser shock peening of thin sections of Ti-6Al4V alloy, Surf. Eng. 19 (2) (2013) 127–133.

[30] A.H. Clauer, D.F. Lahrman, Laser shock processing as a surface enhancement process, Key Eng. Mater. 197 (2001) 121–144.

[31] M. Morales, J.A. Porro, M. Blasco, C. Molpeceres, J.L. Ocaña, Numerical simulation of plasma dynamics in laser shock processing experiments, Appl. Surf. Sci. 255 (10) (2009) 5181–5185.

[32] A. Kadhim, E.T. Salim, S.M. Fayadh, A.A. Al-Amiery, A.A.H. Kadhum, A.B. Mohamad, Effect of multipath laser shock processing on microhardness, surface roughness, and wear resistance of 2024-T3 Al alloy, Sci. World J. 2014 (2014) 6.

[33] P. Peyre, L. Berthe, X. Scherpereel, R. Fabbro, E. Bartnicki, Experimental study of laser-driven shock waves in stainless steels, J. Appl. Phys. 84 (11) (1998) 5985–5992.

[34] R. Fabbro, P. Peyre, L. Berthe, X. Scherpereel, Physics and applications of lasershock processing, J. Laser Appl. 10 (6) (1998) 265–279.

[35] T.S. Kuan, R.R. Ahrens, S.L. Sass, The stress-induced omega phase transformation in Ti-V alloys, Metall. Trans. A. 6 (9) (1975) 1767–1774.

[36] F. Sun, J.Y. Zhang, M. Marteleur, T. Gloriant, P. Vermaut, D. Laillé, P. Castany, C. Curfs, P.J. Jacques, F. Prima, Investigation of early stage deformation mechanisms in a metastable β titanium alloy showing combined twinning-induced plasticity and transformation-induced plasticity effects, Acta Mater. 61 (17) (2013) 6406–6417.

[37] S. Hanada, O. Izumi, Deformation behaviour of retained β phase inβ-eutectoid Ti-Cr alloys, J. Mater. Sci. 21 (12) (1986) 4131–4139.

[38] S. Hanada, O. Izumi, Transmission electron microscopic observations of mechanical twinning in metastable beta titanium alloys, Metall. Trans. A. 17 (8) (1986) 1409–1420.

[39] E. Sukedai, M. Shimoda, H. Nishizawa, Y. Nako, Nucleation behaviour of β to ω phase transformations in β-type Ti-Mo alloys, Mater. Trans. 52 (3) (2011) 324–330.

[40] M.J. Lai, C.C. Tasan, J. Zhang, B. Grabowski, L.F. Huang, D. Raabe, Origin of shear induced β to ω transition in Ti–Nb-based alloys, Acta Mater. 92 (2015) 55–63.

[41] X. Zhao, M. Niinomi, M. Nakai, J. Hieda, Effect of deformation-induced ω phase on the mechanical properties of metastable β-type Ti-V alloys, Mater. Trans. 53 (8) (2012) 1379–1384.
[42] H. Liu, M. Niinomi, M. Nakai, K. Cho, Athermal and deformation-induced ω-phase transformations in biomedical beta-type alloy Ti–9Cr–0.2O, Acta Mater. 106 (2016) 162–170.
[43] M. Ahmed, D. Wexler, G. Casillas, D.G. Savvakin, E.V. Pereloma, Strain rate dependence of deformation-induced transformation and twinning in a metastable titanium alloy, Acta Mater. 104 (2016) 190–200.
[44] D. Devaux, R. Fabbro, L. Tollier, E. Bartnicki, Generation of shock waves by laserinduced plasma in confined geometry, J. Appl. Phys. 74 (4) (1993) 2268–2273.
[45] S. Banerjee, R. Tewari, G.K. Dey, Omega phase transformation – morphologies and mechanisms, Int. J. Mater. Res. 97 (7) (2006) 963–977.
[46] N. Maury, B. Denand, M. Dehmas, C. Archambeau-Mirguet, J. Delfosse, E. AebyGautier, Influence of the ageing conditions and the initial microstructure on the precipitation of α phase in Ti-17 alloy, J. Alloys Compd. 763 (2018) 446–458.

Table 1
Chemical composition of Ti-17 alloy

Element	Al	Sn	Zr	Mo	Cr	Ti
wt%	4.5–5.5	1.6–2.4	1.6–2.4	3.5–4.5	3.5–4.5	Bal

Figure captions

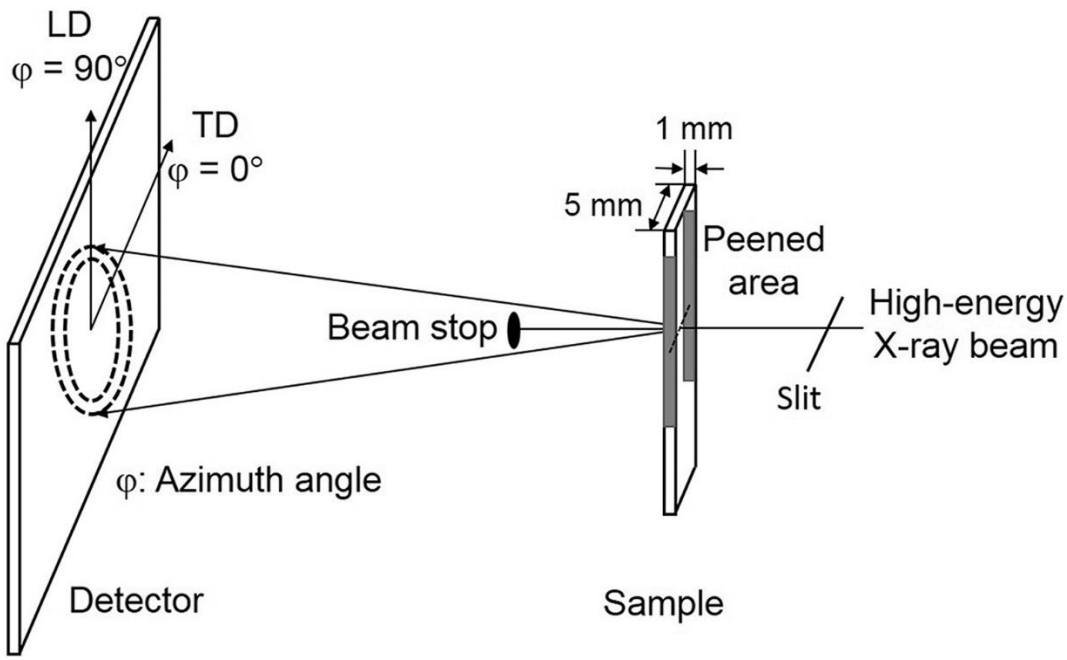

Fig. 1. Schematic geometry of the experimental set-up of in situ HE-XRD measurement.

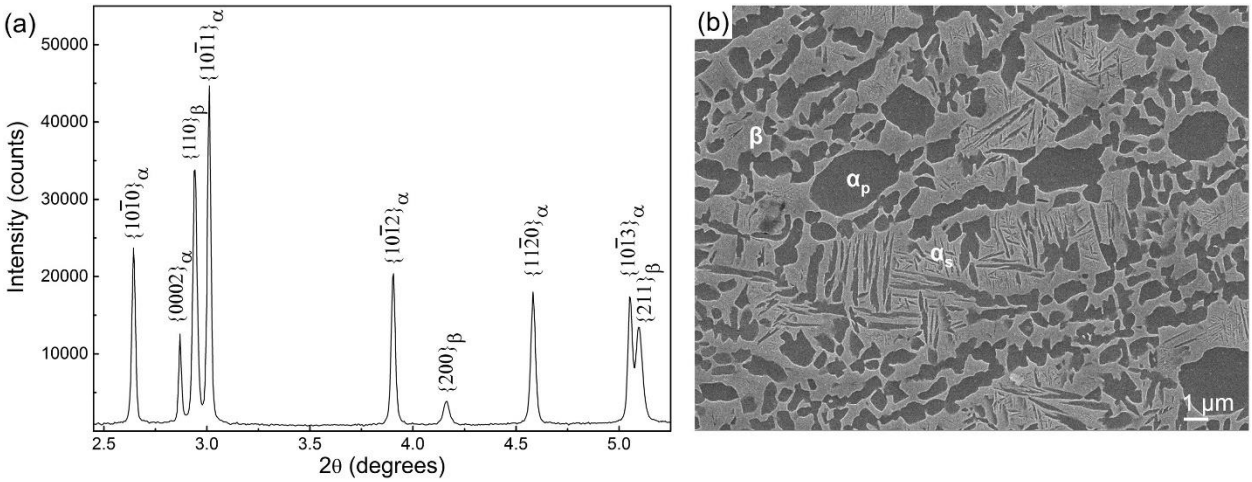

Fig. 2. (a) 1D HE-XRD profile integrated over the entire 360° azimuthal range and (b) SEM micrograph of the original material.

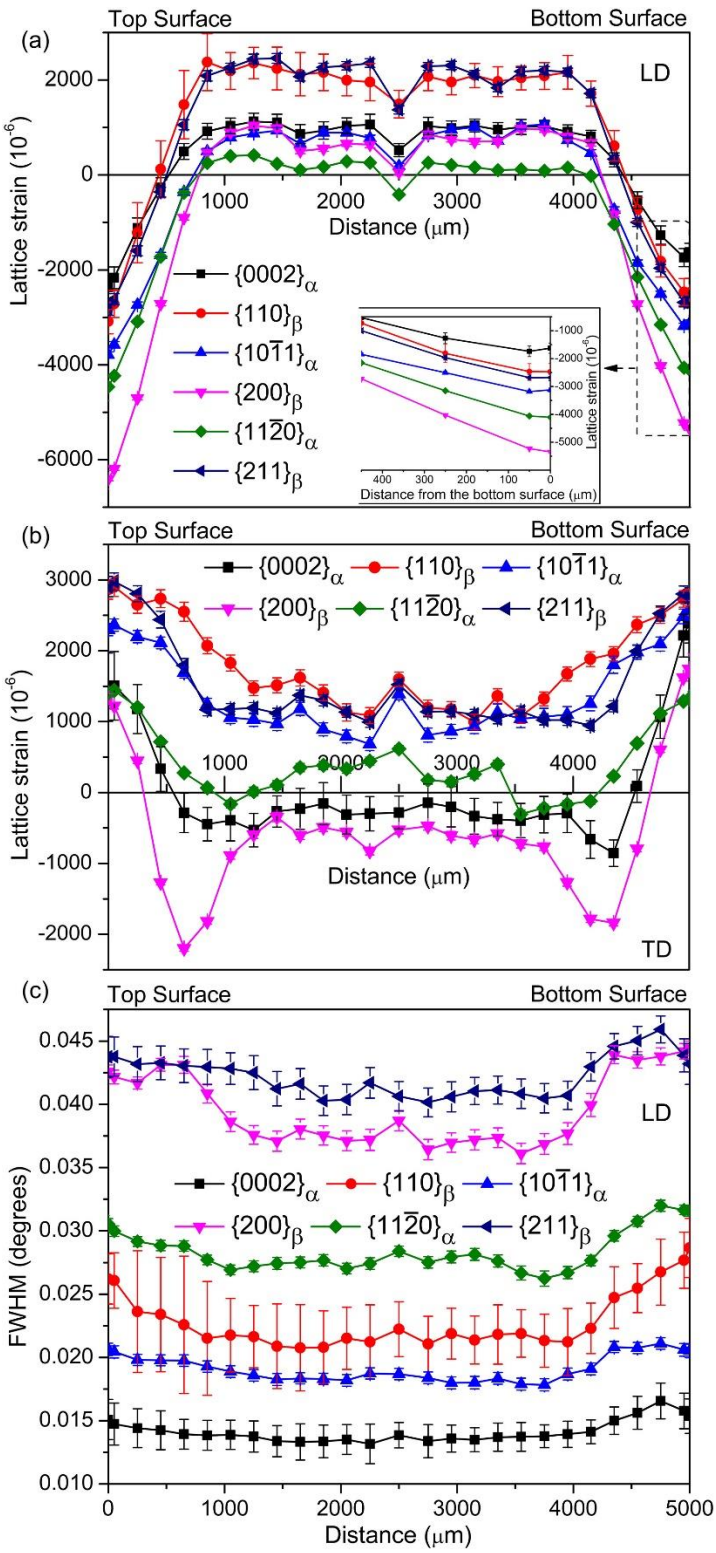

Fig. 3. Measured in-depth residual lattice strain profiles along the LD (a) and the TD (b), and in-depth FWHM profiles along the LD (c).

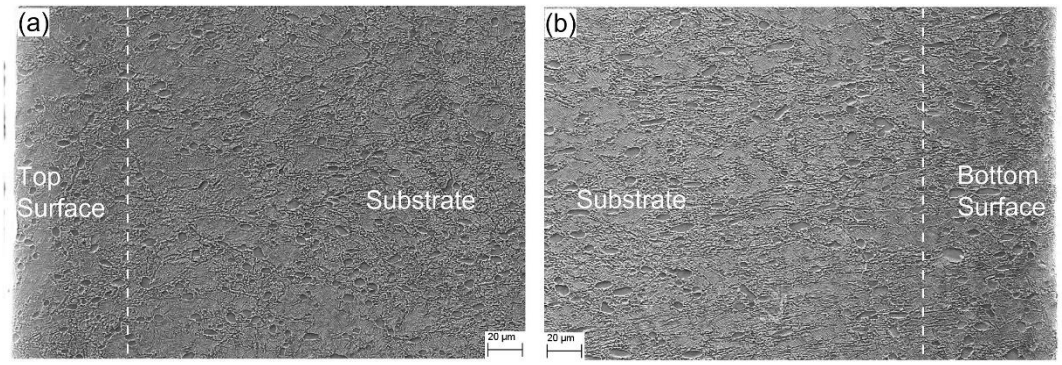

Fig. 4. Cross-sectional SEM micrographs near the top surface (a) and the bottom surface (b) of the LSP-treated sample.

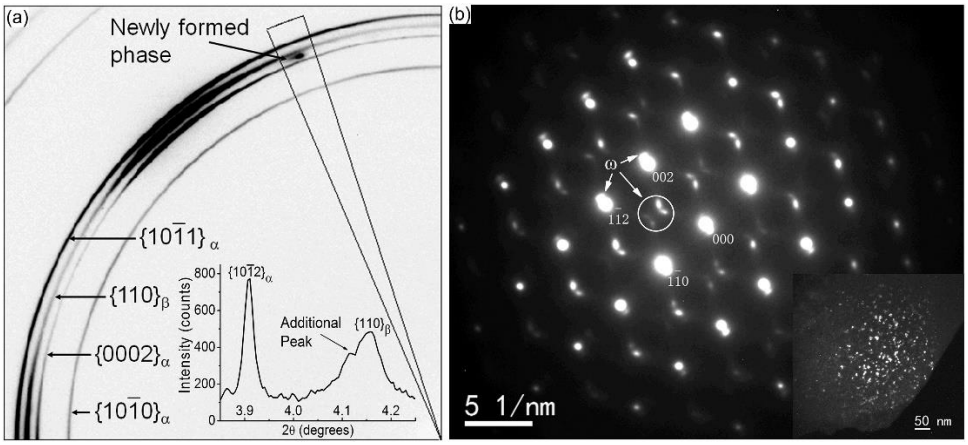

Fig. 5. (a) 2D HE-XRD pattern of the bottom surface and (b) electron diffraction pattern from the ⟨110⟩$_\beta$ zone axis and the corresponding dark-field electron micrograph.

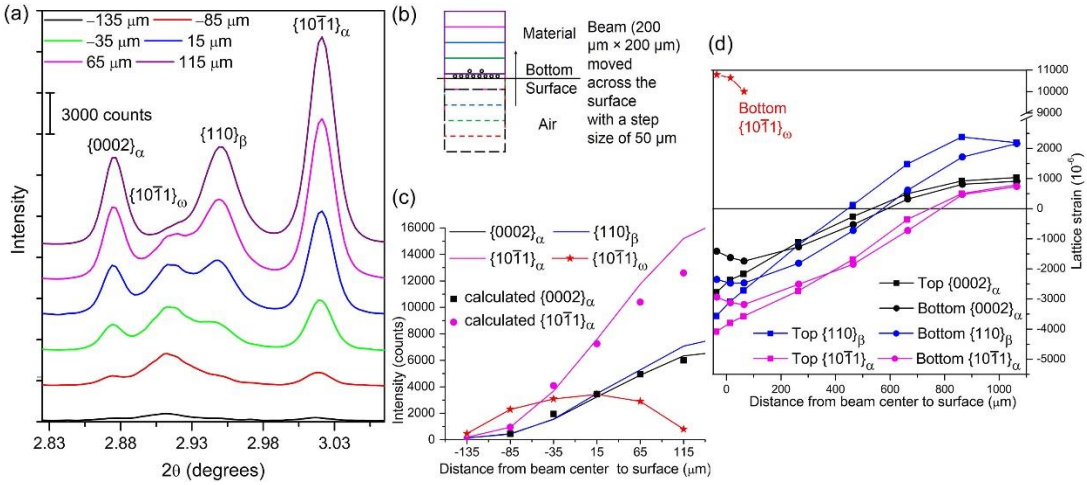

Fig. 6. (a) 1D HE-XRD profiles integrated along the specific azimuth angle as shown in Fig. 5(a). (b) Schematic route of beam movement near the bottom surface. (c) Evolution of integral intensities of three phases near the bottom surface. (d) Comparison of the lattice strains of different planes in the LD on both sides.